Angewandte Chemie
Eine Zeitschrift der Gesellschaft Deutscher Chemiker

Supporting Information

Introducing 4*s*–2*p* Orbital Hybridization to Stabilize Spinel Oxide Cathodes for Lithium-Ion Batteries

G. Liang, E. Olsson, J. Zou, Z. Wu, J. Li, C.-Z. Lu, A. M. D'Angelo, B. Johannessen, L. Thomsen, B. Cowie, V. K. Peterson, Q. Cai, W. K. Pang, Z. Guo**

Experimental methods

1. Material synthesis

Spinel-type LNMO and 4*s*-LNMO with the chemical formula of $LiNi_{0.5}Mn_{1.5}O_4$ and $LiNi_{0.5}Mn_{1.48}Ge_{0.02}O_4$, respectively, were successfully synthesized using a solid-state reaction. All chemicals were purchased from Sigma-Aldrich® and used without further purification. In a typical process, stoichiometric amounts of MnO_2, NiO, Li_2CO_3, and GeO_2 were mixed homogeneously by ball-milling at 400 revolutions per minute for 20 h. Subsequently, the mixture was calcined in air at 850 ℃ for 10 h with a ramping rate of 5 ℃ per minute.

2. Material characterization

The particle size and morphology of the spinel active materials were investigated on the scanning electron microscopy (SEM, JEOL JSM 7500) and aberration-corrected transmission electron microscopy (TEM, JEOL ARM-200F) instruments. Energy dispersive spectroscopy (EDS) was carried out on the SEM JEOL JSM 7500 to probe the element distribution within the material particles. The TEM specimen was processed by cross-sectional focused ion beam (FIB) on an FEI Helios Nanolab instrument with a Ga^+ ion beam to achieve a thin and uniform sample thickness. To further investigate the crystal structure of the Ge-doped LNMO, scanning TEM was carried out in high-angle annular dark-field (HAADF) mode on the JEOL ARM-200F equipment. X-ray photoelectron spectroscopy (XPS) characterization was performed using a Thermo Fisher KAlpha system. All the recorded data were calibrated by C 1*s* peak position at 284.8 eV.[1] Ge *K* edge X-ray absorption spectroscopy (XAS) spectra were collected at the wiggler XAS Beamline (12ID), Australian Synchrotron, in transmission mode, where GeO_2 and metallic Ge were employed as references of Ge^{4+} and Ge^{0+}, respectively.

Both LNMO and 4*s*-LNMO were characterized by X-ray powder diffraction (XRPD) using a PANalytical Empyrean instrument with Cu Kα radiation and neutron powder diffraction (NPD) at two wavelengths using Echidna[2] at the Open Pool Australian Light water (OPAL) research reactor at the Australian Nuclear Science and Technology Organisation (ANSTO). The wavelengths of the neutron beam were determined to be 1.62147(2) and 2.43853(4) Å by using

the $La^{11}B_6$ National Institute of Standards and Technology (NIST) standard reference material 660b. NPD data were recorded in the 2θ range of 4-164° with a step size of 0.05°. GSAS-II software[3] was used to perform Rietveld analysis against both XRPD and NPD data, where refined parameters included the zero shift, peak shape parameters, background coefficients, lattice parameters, oxygen positional parameters, site occupancy factors, scale factors, and isotropic atomic displacement parameters (U_{iso}).

3. Electrochemical characterization

Cathodes were fabricated by mixing LNMO or 4*s*-LNMO with carbon black (Super P) and polyvinylidene difluoride (PVDF) in a weight ratio of 80:10:10, respectively, in the N-methyl-2-pyrrolidone (NMP) solution. The uniform slurry was then pasted onto the Al foil using a doctor blade and dried at 120 °C for 12 h under vacuum. Subsequently, the electrode was cut into disks and pressed before the assembly of the batteries. CR 2032-type coin cells were assembled in an Ar-filled glovebox using Li foil, Celgard® 2400 polypropylene film, and 1 M $LiPF_6$ in the mixture of ethylene carbonate (EC) and dimethyl carbonate (DMC) (1:1 volume ratio) as the counter electrode, separator, and electrolyte, respectively. The assembled cells were galvanostatically charged and discharged on the Land 2001A cell test system in the voltage range of 3.5-4.9 V (vs. Li) at room temperature. Cyclic voltammetry (CV) measurements were carried out on a VMP3 electrochemical workstation at different scan rates between 3.5 and 4.9 V.

The lithium diffusion coefficient (D_{Li}) was calculated using the Randles-Sevcik equation[4], i.e.,

$$i_p = (2.69*10^5)\, n^{3/2}\, A\, D_{Li}^{1/2}\, v^{1/2}\, \Delta C_{Li}$$

where i_p corresponds to the peak current (A), n represents the number of electrons per reaction species, A is the surface area of the tested electrode, D_{Li} is the apparent diffusion coefficient of Li ($cm^2\ s^{-1}$), v is the scan rate ($V\ s^{-1}$), and ΔC_{Li} is the change in lithium-ion concentration ($mol\ cm^{-3}$).

4. Mechanistic studies based on synchrotron techniques

In operando synchrotron-based X-ray powder diffraction measurements were performed at the Powder Diffraction beamline of Australian Synchrotron, Melbourne, Australia. Customized batteries were employed in the experiments using our previous preparation method.[5] The wavelength of the synchrotron beam was determined to be 0.688762(1) Å using the $La^{11}B_6$ NIST standard reference material 660b. Previously-uncycled batteries containing unmodified LNMO and 4*s*-LNMO cathodes were tested at 0.1 C between 3.5 and 4.9 V (1 C = 147 mA g^{-1}, 0.1 C corresponds to 10 h for a single charge or discharge process). Previously-cycled cells were measured at a higher current density of 0.2 C. During the battery testing, the diffraction data were recorded by an MYTHEN microstrip detector[6] with the acquisition and interval time of 60 and 350 s, respectively. Sequential Rietveld refinement analysis using the diffraction data was performed using the GSAS-II software with initial structural details as shown in **Table S1**. The refined parameters included lattice parameters and weight fractions. The weighted profile R-factor R_{wp} of the sequential refinement results varies between 2.28 and 2.76%. *Ex situ* near-edge X-ray absorption fine structure (NEXAFS) studies were carried out in total electron yield (TEY) mode at the soft X-ray beamline, Australian Synchrotron.[7] We note that the TEY mode has a detection depth of around 5 nm from the particle surface. The electrodes used in the experiments were first extracted from coin cells and cleaned with DMC solution before use. The corresponding data were processed using Igor Pro 8 software, with the help of QANT, which was developed at Australian Synchrotron.[8]

5. First-principles calculations

Density functional theory (DFT) calculations were performed in the Vienna ab initio simulation package (VASP) to assess the electronic structure of LNMO and modified LNMO with Ge at different Wyckoff sites and their impact on oxygen vacancy formation.[9] The projector-augmented wave method[10] was applied for the ion-electron interactions and Perdew-Burke-Enzerhof (PBE)[11] functionals. After convergence, a plane-wave cut-off of 600 eV was selected, and a 4 x 4 x 4 Γ-centred Monkhorst-Pack[12] grid was used to simulate the LNMO (containing 56 atoms), and a Γ-point Monkhorst-Pack grid was used for the Ge-doped LNMO (containing 448 atoms). The electronic and ionic self-consistence criteria were 10^{-5} eV and 10^{-3} eV $Å^{-1}$, respectively. To account for the on-site Columbic interaction of Mn and Ni 3*d* electrons, we employed DFT+U

using Dudarev's approach.[13] Based on previous studies, the Hubbard parameters (Ueff) for Mn and Ni were chosen to be 5 and 6 eV, respectively.[14] Bader charges were calculated using the Henkelman algorithm.[15]

The LNMO cell was generated from the experimental data (**Table S1**) using the supercell code[16] to probe the Ni/Mn configuration. The lowest energy configuration was then expanded to study Ge doping at 16*c* and 16*d* sites, respectively. To model Ge dopant on either a 16*c* or 16*d* site, one Mn was substituted by a Ge, and the defect formation energy (E_f) was calculated by[17]

$$E_f = E_{Defective} - E_{Bulk} + \sum n_j \mu_j$$

Where $E_{Defective}$ is the total energy of the LNMO bulk with Ge at either a 16*c* or 16*d* site, E_{Bulk} is the total energy of the undoped LNMO bulk, *j* is the species added or removed between the undoped and Ge-doped LNMO (*j* is either Ge or Mn, as Ge doping here is a substitutional defect at a Mn site), n_j is the number of removed or added species (n = 1), and μ_j is the chemical potential of species *j*. Here, the chemical potentials for Ge and Mn are taken from their metallic bulk.

$E_{f(vac)}$ denotes the oxygen vacancy formation energy, where E_{Bulk} is the total energy of the Ge-containing LNMO, $E_{Defective}$ corresponds to the total energy of Ge-containing LNMO with an oxygen vacancy, and μ_j is taken as half the total energy of an oxygen molecule in vacuum.

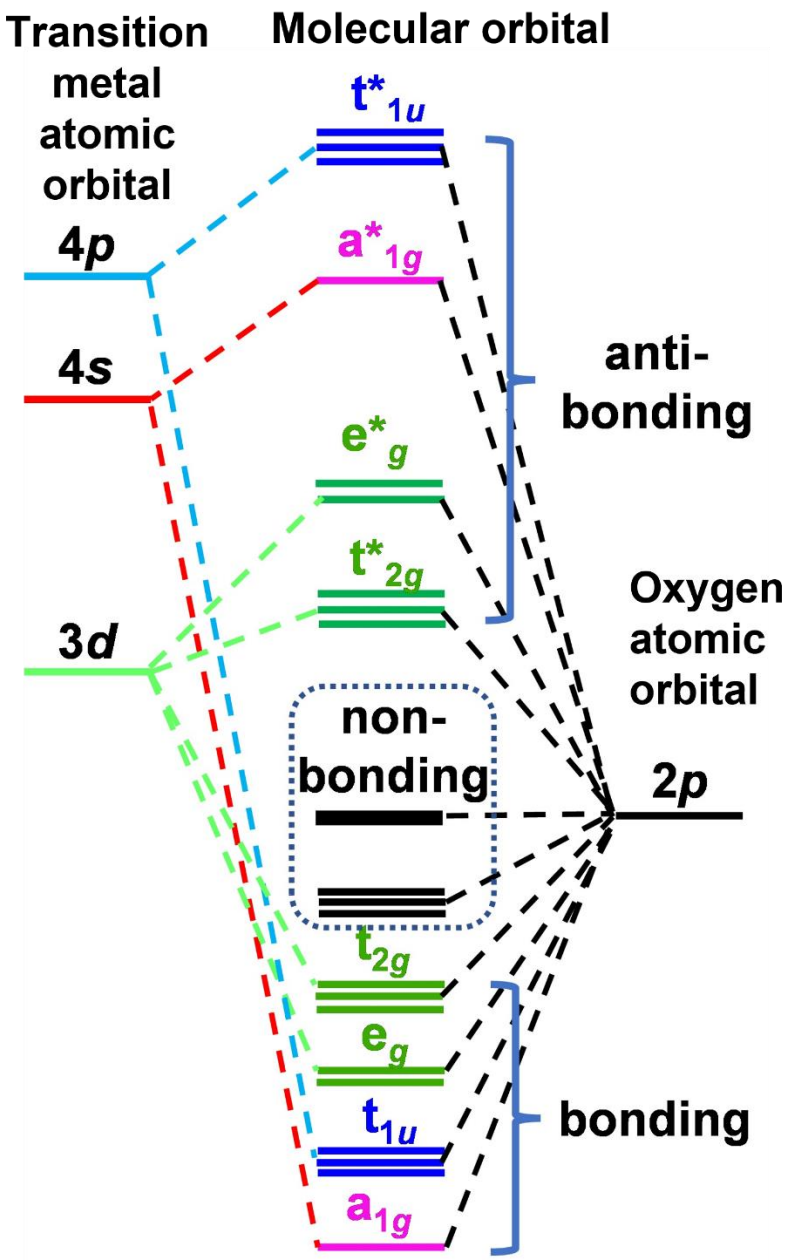

Figure S1. Qualitative schematic of molecular orbital energies of oxides with six-coordinate O forming octohedra with O_h point group.[18]

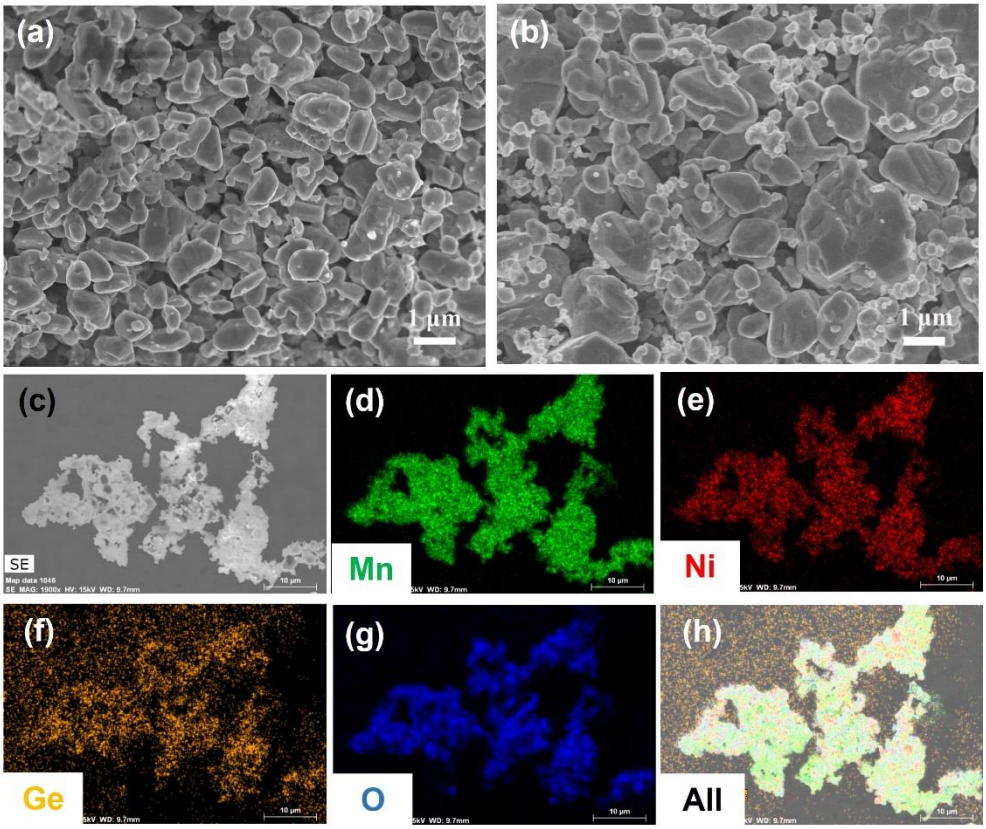

Figure S2. SEM images of (a) LNMO and (b) 4*s*-LNMO; (c) SEM image of 4*s*-LNMO and corresponding elemental mapping using energy-dispersive X-ray spectroscopy for (d) Mn, (e) Ni, (f) Ge, (g) O, and (h) all elements.

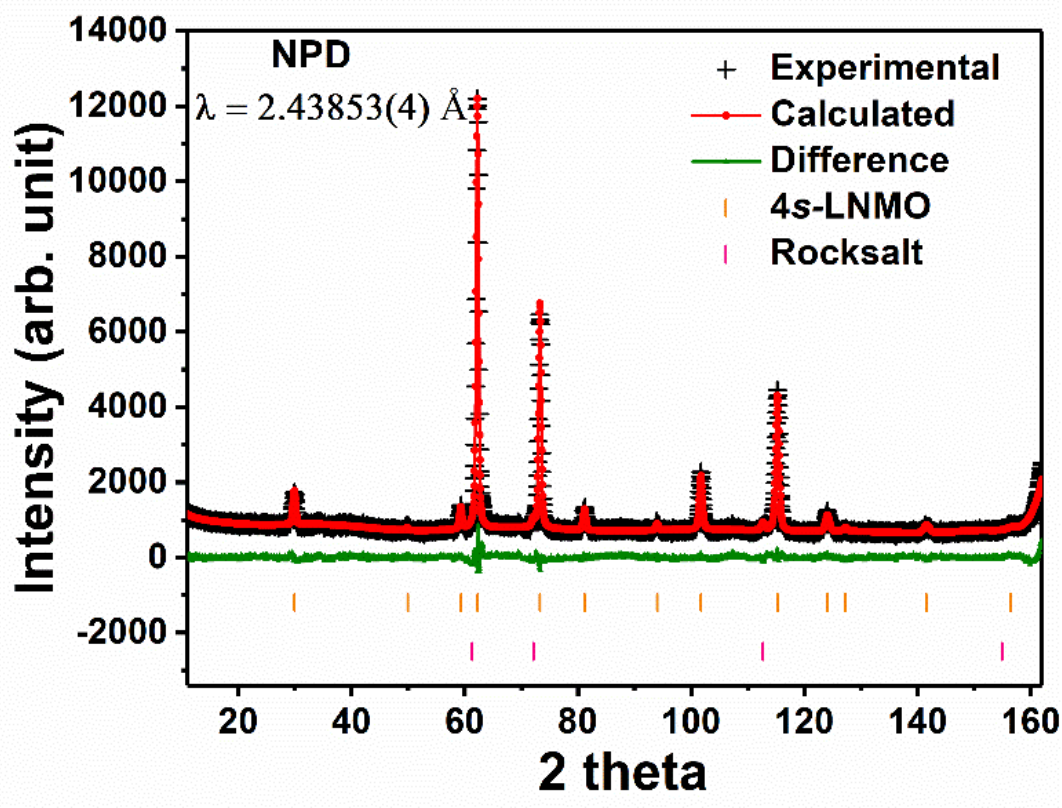

Figure S3. Joint Rietveld refinement profiles of 4*s*-LNMO using NPD data with a wavelength of 2.43853(4) Å.

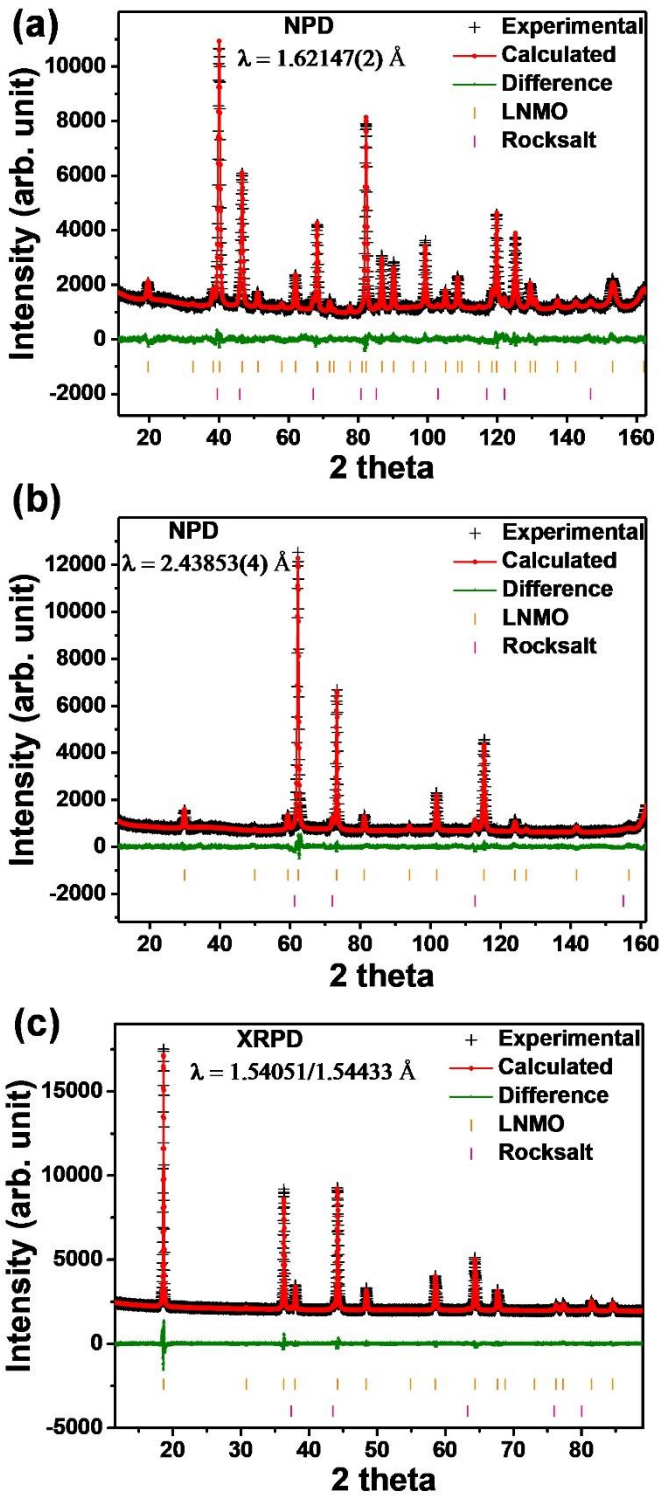

Figure S4. Joint Rietveld refinement profiles using (a) and (b) NPD data at different neutron wavelengths and (c) XRPD data of LNMO (weighted profile R-factor R_{wp} = 5.14%, combined goodness-of-fit GOF = 1.51).

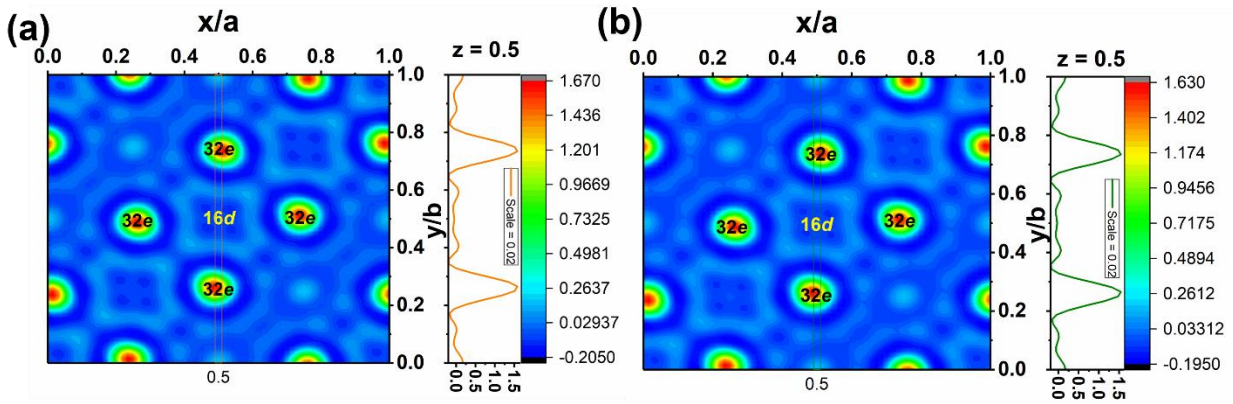

Figure S5. Nuclear density contour map obtained from NPD of (a) LNMO and (b) 4*s*-LNMO with intensity shown in color with the legend given, with the summation along a = 0.5 shown on the right.

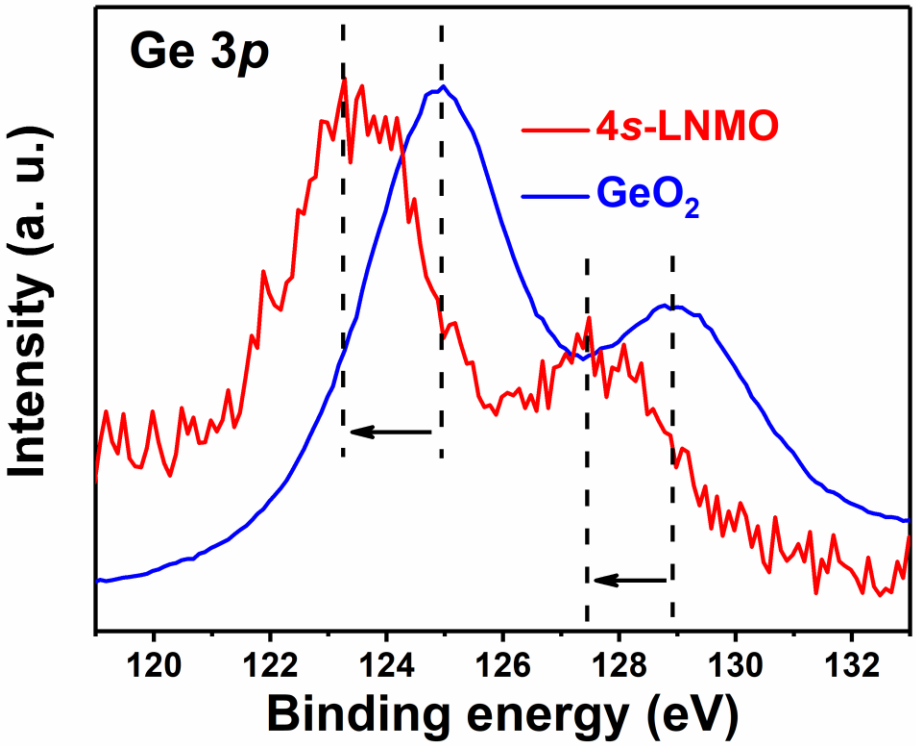

Figure S6. Ge 3*p* XPS data of 4*s*-LNMO and GeO_2.

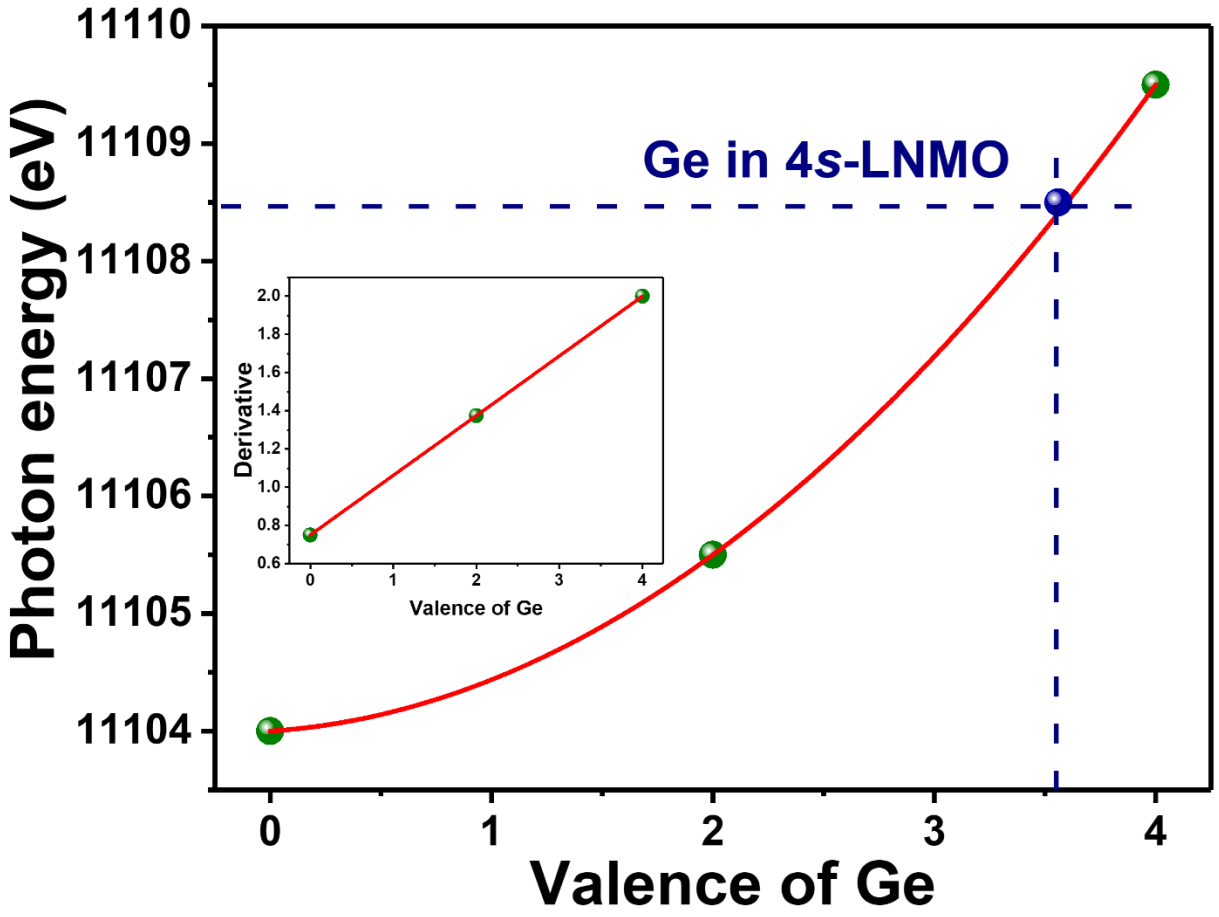

Figure S7. Calibration of Ge *K* edge of Ge with different valence states, where the Ge^{2+} energy is obtained from ref. [19] and Ge^{0} and Ge^{4+} energies are obtained from the first derivative (dμ(E)/dE) of the XAS data. The inset shows the corresponding derivative of the fitting results.

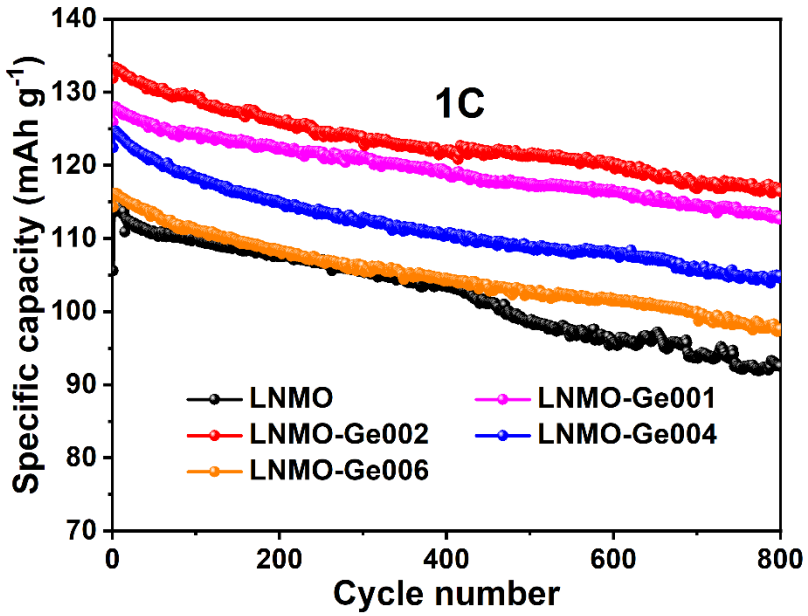

Figure S8. Comparison of battery performance of LNMO with different Ge concentrations. Note that the LNMO-Ge*x* notation corresponds to the chemical formula of $LiNi_{0.5}Mn_{1.5-x}Ge_xO_4$.

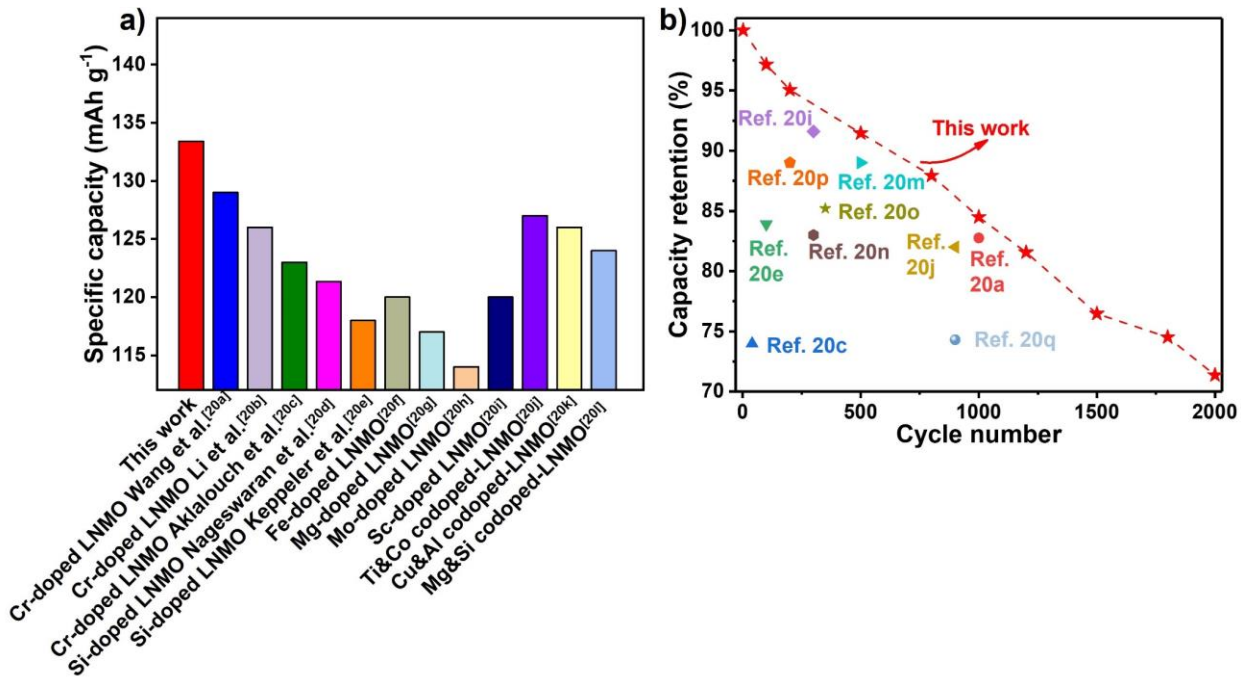

Figure S9. Comparison of the (a) specific capacity and (b) capacity retention of different LNMO materials[20] at 1 C.

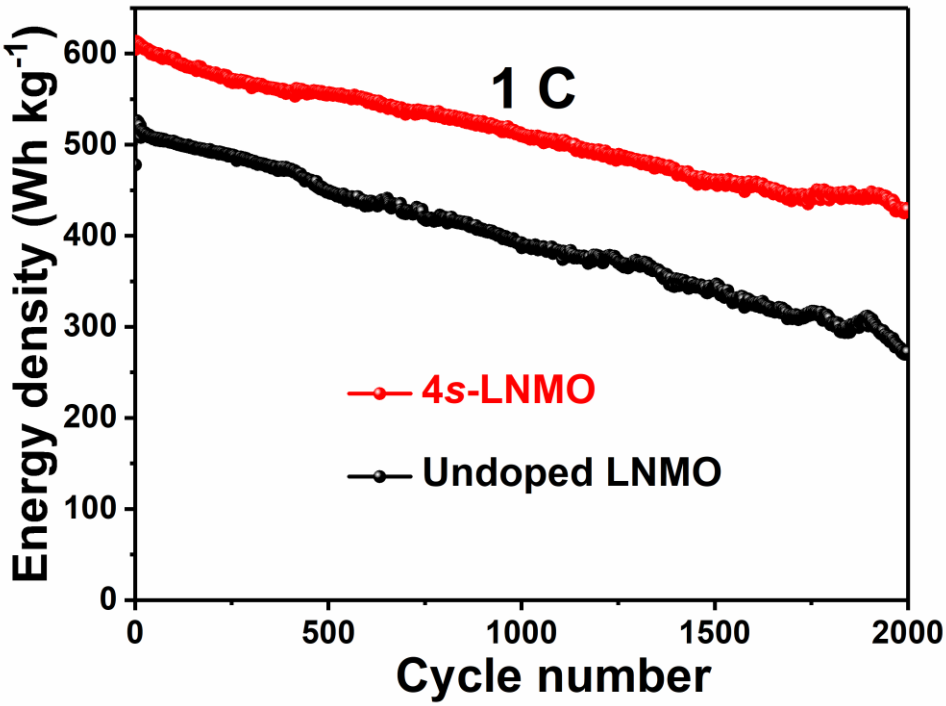

Figure S10. Energy density of LNMO and 4*s*-LNMO at 1 C during cycling.

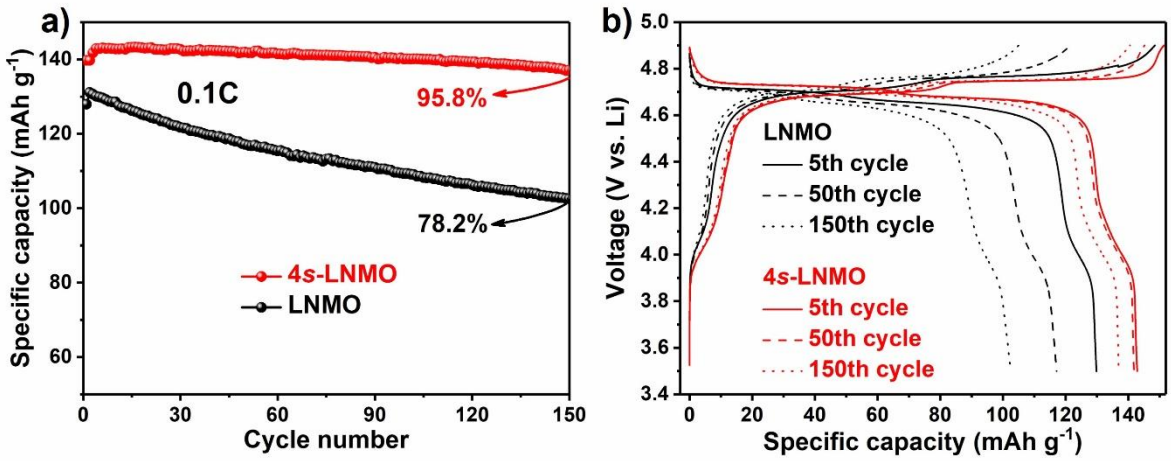

Figure S11. (a) Cycling performance of LNMO and 4*s*-LNMO at 0.1 C and (b) corresponding charge/discharge curves of both samples in the 5th, 50th, and 150th cycles.

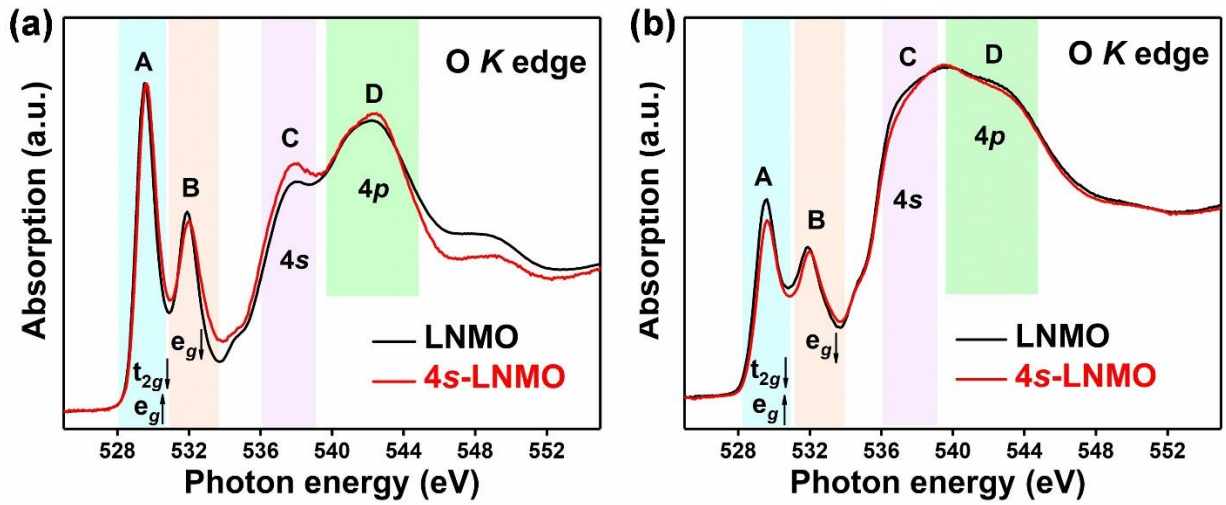

Figure S12. O *K* edge near-edge X-ray absorption fine structure (NEXAFS) spectra of LNMO and 4*s*-LNMO at (a) OCV and (b) fully charged state.

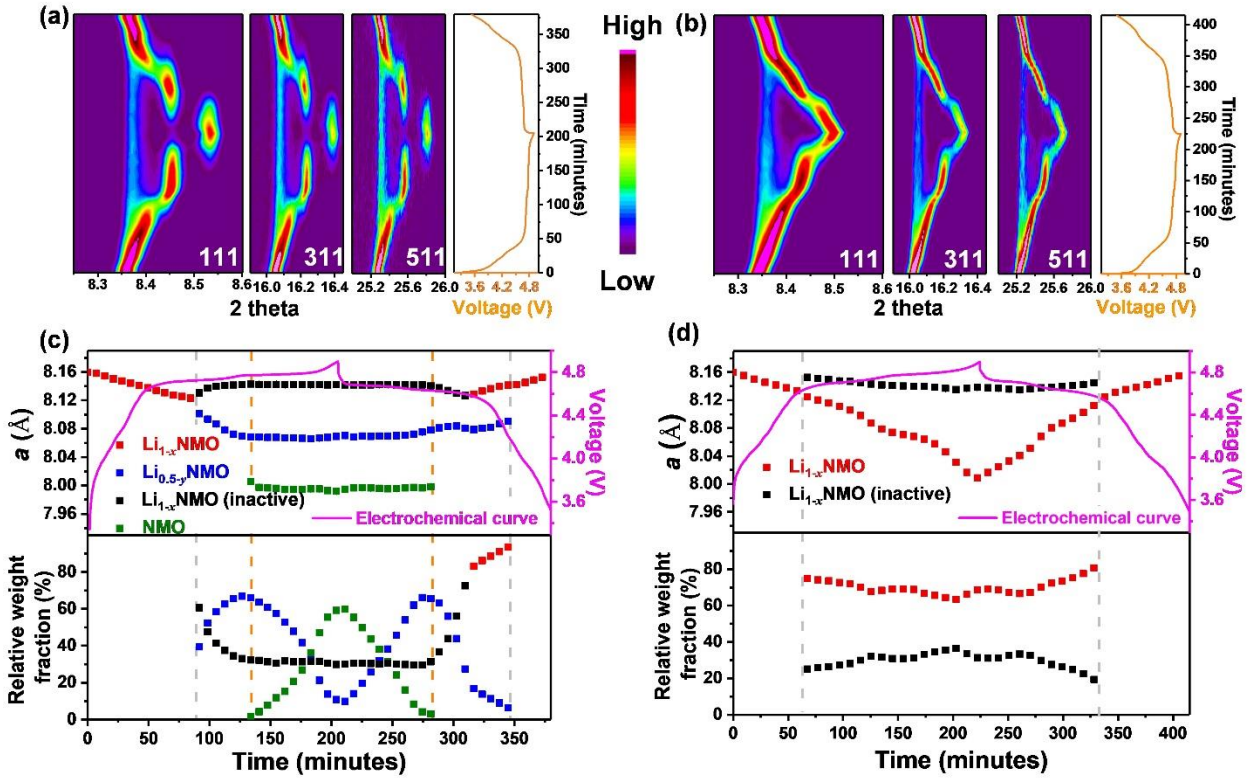

Figure S13. *In operando* sXRPD data in selected 2-theta regions shown as a contour map with intensity in color, corresponding to 111, 311, 511 reflections of the spinel-type (a) LNMO and (b) 4*s*-LNMO during the 50th cycle along with the corresponding electrochemical data; evolution of lattice parameter and phase composition, obtained from sequential Rietveld refinements using *in operando* sXRPD data of (c) LNMO and (d) 4*s*-LNMO during the 50th cycle, alongside their corresponding electrochemical data. Standard errors are smaller than the points.

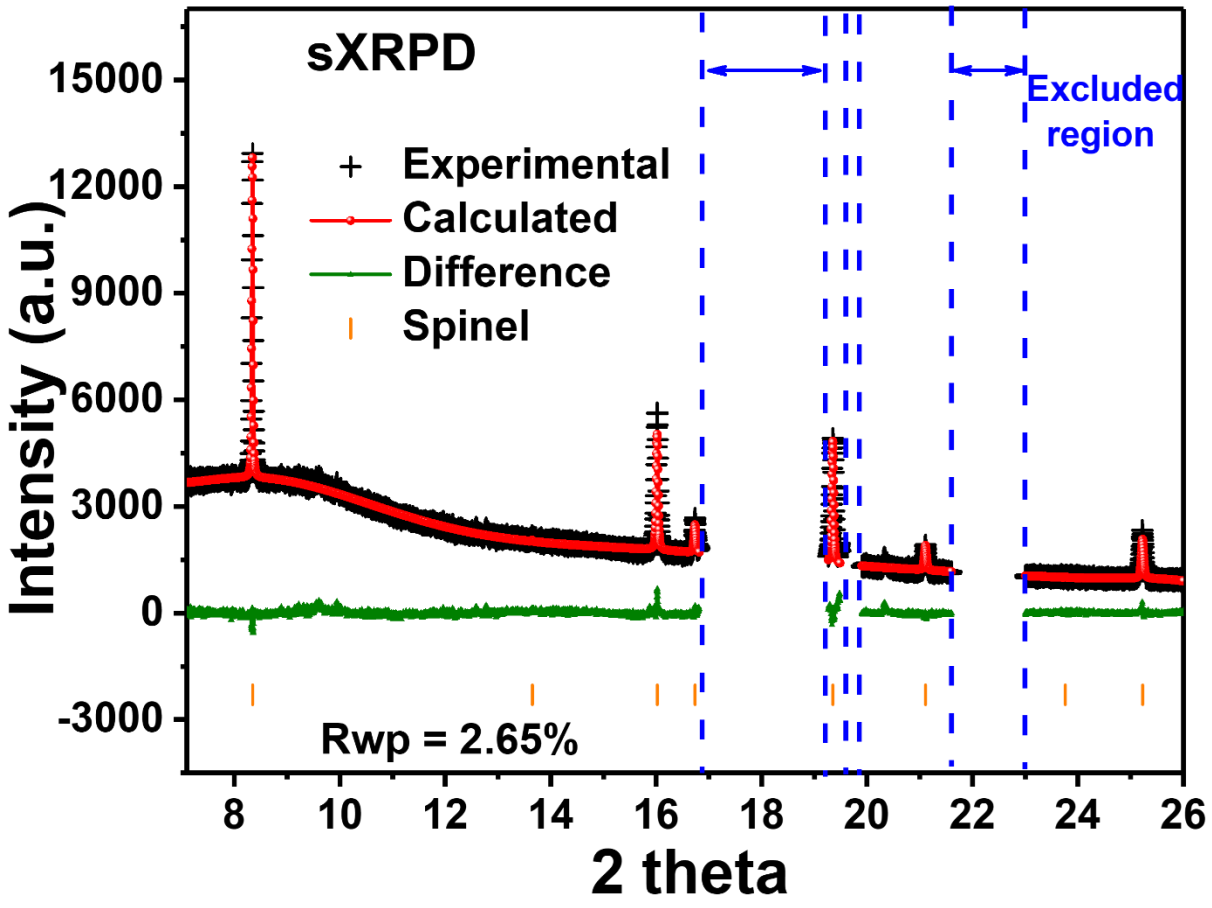

Figure S14. Typical Rietveld refinement profile using *in operando* sXRPD data of the 4*s*-LNMO-containing battery, where R_{wp} represents the weighted profile R-factor.

Table S1. Phase composition and crystallographic details of LNMO and 4*s*-LNMO obtained from joint Rietveld refinement using XRPD data and NPD data at two neutron wavelengths, and the Li-O TM-O bond length.

	Spinel	**Rocksalt ($Li_xNi_{2-x}O_2$)**
LNMO	98.47(3) wt.%	1.53(3) wt.%
4*s*-LNMO	99.26(2) wt.%	0.74(2) wt.%

LNMO Space group $Fd\bar{3}m$						
a = 8.1638(1) Å, volume = 544.11(3) Å^3						
Atom	**Wyckoff site**	***x***	***y***	***z***	**U_{iso} (Å^2)**	**Site occupancy factor**
Li	8*a*	0.125	0.125	0.125	0.016(1)	1
Ni	16*d*	0.5	0.5	0.5	0.0152(6)	0.210(1) [a]
Mn						0.790(1) [a]
O	32*e*	0.26285(4)	0.26285(4)	0.26285(4)	0.0100(2)	0.988(4)

[a] 16*d* site occupation constrained to be 1.

4*s*-LNMO Space group $Fd\bar{3}m$						
a = 8.16607(9) Å, volume = 544.55(1) Å^3						
Atom	**Wyckoff site**	***x***	***y***	***z***	**U_{iso} (Å^2)**	**Site occupancy factor**
Li	8*a*	0.125	0.125	0.125	0.0144(9)	1
Ni	16*d*	0.5	0.5	0.5	0.0146(6)	0.215(1) [b]
Mn						0.780(1) [b]
Ge						0.005 [b,c]

Ge	16*c*	0	0	0		0.005 [c]
O	32*e*	0.26279(3)	0.26279(3)	0.26279(3)	0.0097(2)	0.981(4)

[b]16*d* site occupation constrained to be 1.

[c] Constrained to be the same.

	Li-O bond length (Å)	**TM-O bond length (Å)**
LNMO	1.94920(18)	1.941767(16)
4*s*-LNMO	1.94890(16)	1.942705(15)

Table S2. Calculated mean bond lengths and mean Bader charges (q) for pristine LNMO, LNMO with Ge at 16*c* sites, and LNMO with Ge at 16*d* sites. For each system, the bond lengths and Bader charges are calculated after removing a single oxygen atom to create an oxygen vacancy (V_O). NN denotes M-O bond next to a V_O.

	LNMO		Ge at 16*c* site		Ge at 16*d* site	
	No V_O	With V_O	No V_O	With V_O	No V_O	With V_O
Li-O bond length (Å)	1.96	1.87 NN, 1.97	1.93	1.81 NN, 1.93	1.98	1.88 NN, 1.99
TM-O bond length (Å)	1.95	1.90 NN, 1.94	1.95	1.85 NN, 1.95	1.97	1.89 NN, 1.98
Ge-O bond length (Å)	N/A	N/A	1.92	1.83 NN, 1.88	1.93	1.80 NN, 1.89
q_{Li} (e)	0.89	0.89	0.89	0.89	0.89	0.89
q_{Mn} (e)	1.79	1.64 NN, 1.81	1.81	1.47 NN, 1.82	1.82	1.66 NN, 1.82
q_{Ni} (e)	1.21	1.18 NN, 1.23	1.20	1.20	1.22	1.21
q_O (e)	-1.06	-1.10	-1.07	-1.07	-1.08	-1.08
q_{Ge} (e)	N/A	N/A	2.29	2.23	2.36	2.23

Reference:

[1] a) F. Yang, J. Hao, J. Long, S. Liu, T. Zheng, W. Lie, J. Chen, Z. Guo, *Adv. Energy Mater.* **2020**, *11*, 2003346; b) G. Liang, Z. Wu, C. Didier, W. Zhang, J. Cuan, B. Li, K.-Y. Ko, P.-Y. Hung, C.-Z. Lu, Y. Chen, G. Leniec, S. M. Kaczmarek, B. Johannessen, L. Thomsen, V. K. Peterson, W. K. Pang, Z. Guo, *Angew. Chem. Int. Ed.* **2020**, *59*, 10594-10602; c) H. Liu, W. Pei, W.-H. Lai, Z. Yan,

H. Yang, Y. Lei, Y.-X. Wang, Q. Gu, S. Zhou, S. Chou, H. K. Liu, S. X. Dou, *ACS Nano* **2020**, *14*, 7259-7268.
[2] K.-D. Liss, B. Hunter, M. Hagen, T. Noakes, S. Kennedy, *J. Phys. B* **2006**, *385*, 1010-1012.
[3] B. H. Toby, R. B. Von Dreele, *J. Appl. Crystallogr.* **2013**, *46*, 544-549.
[4] a) H. Liu, W.-H. Lai, H.-L. Yang, Y.-F. Zhu, Y.-J. Lei, L. Zhao, J. Peng, Y.-X. Wang, S.-L. Chou, H.-K. Liu, *Chem. Eng. J.* **2021**, *408*, 127348; b) H. Liu, J. Wang, X. Zhang, D. Zhou, X. Qi, B. Qiu, J. Fang, R. Kloepsch, G. Schumacher, Z. Liu, J. Li, *ACS Appl. Mater. Interfaces* **2016**, *8*, 4661-4675; c) C. Yin, H. Zhou, Z. Yang, J. Li, *ACS Appl. Mater. Interfaces* **2018**, *10*, 13625-13634.
[5] G. Liang, J. Hao, A. M. D'Angelo, V. K. Peterson, Z. Guo, W. K. Pang, *Batteries Supercaps* **2021**, *4*, 380-384.
[6] K. S. Wallwork, B. J. Kennedy, D. Wang, *AIP Conf. Proc.* **2007**, *879*, 879-882.
[7] B. Cowie, A. Tadich, L. Thomsen, *AIP Conf. Proc.* **2010**, *1234*, 307-310.
[8] E. Gann, C. R. McNeill, A. Tadich, B. C. Cowie, L. Thomsen, *J. Synchrotron Rad.* **2016**, *23*, 374-380.
[9] a) G. Kresse, J. Hafner, *Phys. Rev. B* **1993**, *47*, 558; b) G. Kresse, J. Hafner, *Phys. Rev. B* **1994**, *49*, 14251; c) G. Kresse, J. Furthmüller, *Comput. Mater. Sci.* **1996**, *6*, 15-50; d) G. Kresse, J. Furthmüller, *Phys. Rev. B* **1996**, *54*, 11169.
[10] P. E. Blöchl, *Phys. Rev. B* **1994**, *50*, 17953.
[11] a) J. P. Perdew, K. Burke, M. Ernzerhof, *Phys. Rev. Lett.* **1996**, *77*, 3865; b) J. P. Perdew, K. Burke, M. Ernzerhof, *Phys. Rev. Lett.* **1997**, *78*, 1396-1396.
[12] H. J. Monkhorst, J. D. Pack, *Phys. Rev. B* **1976**, *13*, 5188.
[13] S. Dudarev, G. Botton, S. Savrasov, C. Humphreys, A. Sutton, *Phys. Rev. B* **1998**, *57*, 1505.
[14] Y. Chen, Y. Sun, X. Huang, *Comput. Mater. Sci.* **2016**, *115*, 109-116.
[15] a) G. Henkelman, A. Arnaldsson, H. Jónsson, *Comput. Mater. Sci.* **2006**, *36*, 354-360; b) R. F. Bader, *Atoms in Molecules: A Quantum Theory*, Oxford University Press, Oxford, **1990**.
[16] K. Okhotnikov, T. Charpentier, S. Cadars, *J. Cheminform.* **2016**, *8*, 17-33.
[17] S. Zhang, J. E. Northrup, *Phys. Rev. Lett.* **1991**, *67*, 2339.
[18] a) M. Moreno, M. T. Barriuso, J. A. Aramburu, P. Garcia-Fernandez, J. M. Garcia-Lastra, *J Phys Condens Matter* **2006**, *18*, R315-360; b) M. Okubo, A. Yamada, *ACS Appl. Mater. Interfaces* **2017**, *9*, 36463-36472.
[19] M. J. Ward, P. A. Rupar, M. W. Murphy, Y. M. Yiu, K. M. Baines, T. K. Sham, *Chem. Commun.* **2010**, *46*, 7016-7018.
[20] a) J. Wang, P. Nie, G. Xu, J. Jiang, Y. Wu, R. Fu, H. Dou, X. Zhang, *Adv. Funct. Mater.* **2017**, *28*, 1704808; b) J. Li, H. Wang, W. Dong, Z. Shi, W. Xie, H. Qiao, Q. Yu, M. Zhang, J. Hu, L. Yang, J. Hong, *J. Phys. Chem. C* **2018**, *122*, 25229-25236; c) M. Aklalouch, J. M. Amarilla, R. M. Rojas, I. Saadoune, J. M. Rojo, *J. Power Sources* **2008**, *185*, 501-511; d) S. Nageswaran, M. Keppeler, S.-J. Kim, M. Srinivasan, *J. Power Sources* **2017**, *346*, 89-96; e) M. Keppeler, S. Nageswaran, S.-J. Kim, M. Srinivasan, *Electrochim. Acta* **2016**, *213*, 904-910; f) E. Hu, S.-M. Bak, Y. Liu, J. Liu, X. Yu, Y.-N. Zhou, J. Zhou, P. Khalifah, K. Ariyoshi, K.-W. Nam, X.-Q. Yang, *Adv. Energy Mater.* **2016**, *6*, 1501662; g) M.-H. Liu, H.-T. Huang, C.-M. Lin, J.-M. Chen, S.-C. Liao, *Electrochim. Acta* **2014**, *120*, 133-139; h) T. Kazda, J. Vondrák, A. Visintin, M. Sedlaříková, J. Tichý, P. Čudek, *J. Energy Storage* **2018**, *15*, 329-335; i) S. Bhuvaneswari, U. V. Varadaraju, R. Gopalan, R. Prakash, *Electrochim. Acta* **2019**, *327*, 135008; j) Y. Han, Y.-S. Jiang, Y. Xia, L. Deng, L.-F. Que, F.-D. Yu, Z.-B. Wang, *Nano Energy* **2022**, *91*, 106636; k) S. Li, Y. Wei, P. Wang, Y. Feng, W. Liang, H. Ding, X. Cui, *J. Alloys Compd.* **2020**, *820*, 153140; l) X. Shu, H. Zhao, Y. Hu, J. Liu, M. Tan, S. Liu, M. Zhang, Q. Ran, H. Li, X. Liu, *Vacuum* **2018**, *156*, 1-8; m) H. B. Lin, Y. M. Zhang, J. N. Hu, Y. T. Wang, L. D. Xing, M. Q. Xu, X. P. Li, W. S. Li, *J. Power Sources* **2014**, *257*, 37-44; n) X. Fang, N. Ding, X. Y. Feng, Y. Lu, C. H. Chen, *Electrochim. Acta* **2009**, *54*, 7471-7475; o) B. Xiao, H. Liu, J. Liu, Q. Sun, B. Wang, K. Kaliyappan, Y. Zhao, M. N. Banis, Y. Liu, R. Li, T. K. Sham, G. A. Botton, M. Cai, X. Sun, *Adv. Mater.* **2017**, *29*, 1703764; p) J. M. Lim, R. G. Oh,

D. Kim, W. Cho, K. Cho, M. Cho, M. S. Park, *ChemSusChem* **2016**, *9*, 2967-2973; q) J. Chong, S. Xun, X. Song, G. Liu, V. S. Battaglia, *Nano Energy* **2013**, *2*, 283-293.